A Multi-mode Transverse Dynamic Force Microscope - Design, Identification and Control

Kaiqiang Zhang, *Member, IEEE*, Guido Herrmann, *Senior Member, IEEE*, Christopher Edwards, *Senior Member, IEEE*, Massimo Antognozzi, Toshiaki Hatano, Thang Nguyen *, Stuart C. Burgess, and Mervyn Miles

***Abstract*—The transverse dynamic force microscope (TDFM) and its shear force sensing principle permit true non-contact force detection in contrast to typical atomic force microscopes. The two TDFM measurement signals for the cantilever allow, in principle, two different scanning modes of which, in particular, the second presented here permits a full-scale non-contact scan. Previous research mainly focused on developing the sensing mechanism, whereas this work investigates the vertical axis dynamics for advanced robust closed-loop control. This paper presents a new TDFM digital control solution, built on field-programmable gate array (FPGA) equipment running at high implementation frequencies. The integrated control system allows the implementation of online customizable controllers, and raster-scans in two modes at very high detection bandwidth and nano-precision. Robust control algorithms are designed, implemented, and practically assessed. The two realized scanning modes are experimentally evaluated by imaging nano-spheres with known dimensions in wet conditions.**

***Index Terms*—Nano-precision control, Fixed-point implementation, Control arithmetic optimization, Scanning-probe microscopy**

I. Introduction

THE atomic force microscope (AFM) [1] is a powerful tool to investigate biological and inorganic sample surfaces at nano-scale. Advanced control algorithms have been, for instance, developed for vertical tip-sample distance control for AFMs [2]–[4]. However, the interaction between the cantilever-tip and the specimen can lead to damage of delicate specimens in typical AFM scanning modes (contact mode or tapping mode [5], [6]). The transverse dynamic force microscope, also commonly known as the shear force microscope (SFM), was first presented in [7] employing a vertical cylindrical probe. This probe interacts with the confined structured liquid (water) layer usually covering any sample-substrates in ambient or wet environments [8]. The probe-sample interaction is sensed by exciting the probe in a sinusoidal fashion and measuring the probe tip oscillation. This oscillation decreases, the deeper the probe penetrates within the fluid layer. The vertical probe permits a true non-contact force measurement and eliminates the spontaneous jump-to-contact phenomenon of the tip in relation to the surface [9] usually known for AFMs.

In many SFMs, the vertical probe is attached to a tuning fork, which is vibrated at its harmonic frequency to horizontally excite the probe, e.g. [10]–[13]. The varying interaction with the thin liquid layer above the sample results in a dynamic change in the probe oscillation (i.e. amplitude and phase). The most common method to measure the probe tip oscillation signal is to apply a lock-in amplifier or a phase-locked-loop (PLL) by taking the measurement of the tuning fork current [11] or the optical sensors directed at the probe tip [14]. However, the sensing and scanning performance of the SFMs is limited by the tuning forks, and their harmonic frequency (about 33 kHz in [11]–[13]). Consequently, the overall shear-force measurement bandwidth is lower than the excitation frequency of the probe. Moreover, the other limitation of the shear force measurement is the bandwidth of the sensing mechanism for the probe motion detection. Recently, the shear force interaction between a nanowire and the sample achieved a sensing bandwidth of 10 kHz [14] by measuring the reflection of a laser directed at a 200 nm wide nano-wire.

A significant advancement over such sensing schemes, employing an evanescent field based sensing mechanism was developed in 2008 [15], avoiding the use of tuning forks. Little in the way of control was used in the previous scanning applications, e.g. [16]. Without studying the vertical dynamics, the vertical axis was controlled by a manually tuned proportional-integral-derivative (PID) control. The cantilever was kept at a constant height with respect to the sample-holder, scanning only the very top part of the specimens [16]. This established a scan mode for the TDFM, referred to as the constant absolute height (CAH) mode. This will be improved in this paper by considering more advanced control design methods. In previous scanning set-ups like [17] , the oscillation signal was processed by using a PLL [15]–[18]. To simplify the sensing component, a new interaction force measurement method was suggested in [19] taking the average amplitude of the cantilever oscillation. A classical control scheme based on a lag-element was applied in [19] to verify the effectiveness of the rapid amplitude sensing mechanism. The control approach, in principle, is a shear-force-interaction feedback scan mode with the aim of retaining a constant relative height to the sample, i.e. achieving zero cantilever-specimen contact. Prior

This work was supported by the University of Bristol Postgraduate Research Scholarship and EPSRC grants EP/I034882/1 & EP/I034831/1.

K. Zhang, G. Herrmann, S.C. Burgess and T.Hatano have been with the Mechanical Engineering Department at the University of Bristol, U.K.. G. Herrmann is with the University of Manchester from July 2019.

M. Antognozzi and M. Miles are with the School of Physics at the University of Bristol, U.K..

C. Edwards is and T. Nguyen was with the University of Exeter, U.K..

*For correspondence: Thang. Nguyen is with the Faculty of Electrical & Electronics Engineering, Ton Duc Thang University, Vietnam (email: nguyentienthang@tdtu.edu.vn)

IEEE holds the copyright of this open access manuscript.

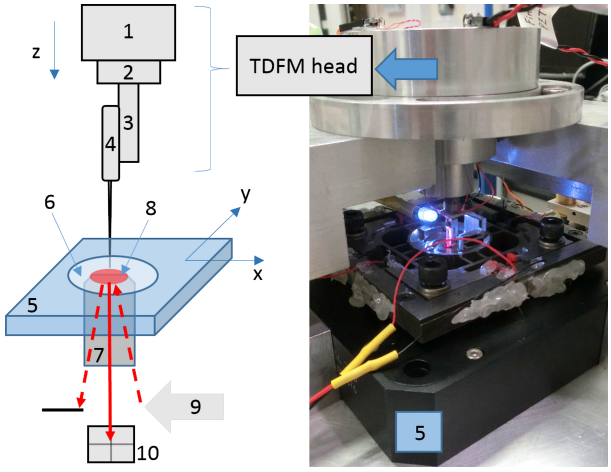

Fig. 1: Schematic of the TDFM: 1) Coarse piezo-actuator; 2) fine piezo-actuator; 3) Dither piezo-ceramic plate; 4) Vertically oriented chip with cantilever probe; 5) Horizontal positioning stage; 6) Transparent sample-holder slide; 7) High numerical aperture lens; 8) Evanescent field; 9) Laser source and optical focusing components; 10) Photo-detector.

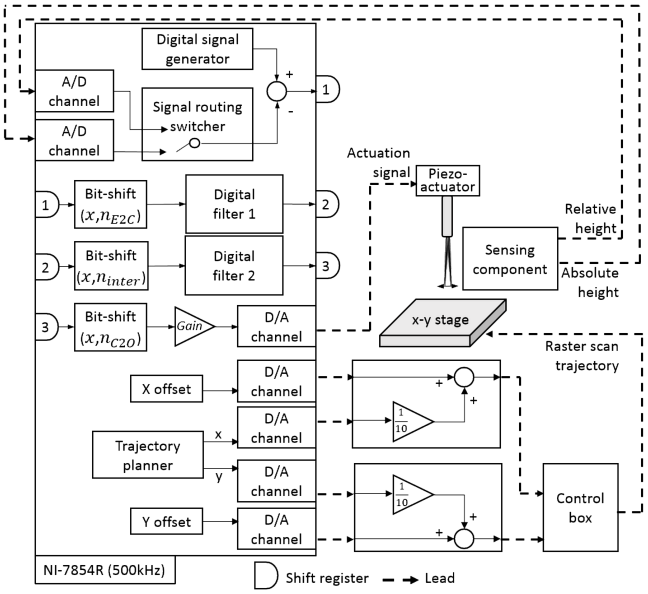

Fig. 2: Electronics design of the FPGA based control solution.

to [19], the scanning mode was limited to specimens less than about 2 nm high, e.g. scanning DNA [17], because the TDFM used to rely on the use of PLL and ad-hoc tuned PID control for shear-force-interaction feedback. Employing a novel optimized FPGA design, this paper will introduce an advanced shear-force-interaction control scheme based on the vertical cantilever positioning dynamics. As a consequence, this work enables a new constant relative height (CRH) scan mode, overcoming the limitation of the specimens' height with improved scan performance. Hence, it has the advantage of staying above the specimens, i.e. obtaining full-scale non-contact images of the whole sample topography.

To achieve the above multi-mode TDFM scanning system, this paper focuses on a novel, efficient, FPGA-based Control and Instrument (C&I) structure. In contrast to previous FPGA control designs ([20], [21]), the proposed design concept allows for online reconfiguration of high-order digital controllers, while guaranteeing an optimized running performance without the need to recompile control programs. The new sensing and control system increases the sensing range, permits system identification, realizes efficient and easily parameterized closed-loop control implementations. In particular, the CRH-mode avoids contact and increases the size of the imaged specimen. In Section II, the TDFM system, i.e. the sensing, basic actuation, and control hardware structure, is introduced. In Section III, the novel sensing system is presented, emphasizing the relevant FPGA-based implementation and optimization. Then, the FPGA based control program is discussed with an optimization method in Section IV. Based on the plant response in the time and frequency domain, two controllers are designed in Section V and VI in a step-wise manner, improving successively the system identification of the system dynamics (including nonlinearity effects which have not been sufficiently studied for control design before). In Section VII, experimental specimen scans are provided for nano-spheres employing the two modes. The comparison of the two scan methods, applied to the same area, shows the advantages of each mode and the success of the integrated TDFM. Section VIII discusses the performance improvements of the proposed TDFM design.

II. The TDFM System

The electronics design (see Figure 2) is developed around field-programmable gate array (FPGA) boards to realize the cantilever sensing mechanism and real-time control for scanning. The TDFM mechanically consists of a horizontal nano-positioning stage and a sensing-actuating component for vertical axis control. The commercial stage (P.734 with E710 controller, Physik Instrumente (PI) GmbH & Co.) carries the sample-substrate to horizontally change the topographic measurement position. A trajectory planner is programmed to generate raster scanning patterns on a National Instrument (NI) 7854R FPGA board. The stage is controlled to follow the imaging raster-scan reference. The vertical z-axis-directed cantilever positioning system exploits the evanescent field based sensing mechanism to provide measurement of the sample-substrate topography at a horizontal x-y position (see Figure 1). The sensing mechanism is implemented on a separate, faster and more powerful FPGA-board, NI7962R, to deal with the high-frequency cantilever dynamics and to permit better use of available FPGA resources (see Figures 2 and 3).

In this paper, all the work is conducted in a wet environment created by ultra-pure water on a grade 0 glass slide (sample-holder). In Figure 1, the optical path is carefully designed following the principle described in [15]. The inlet laser is adjusted, by tuning a complex optical path, to be totally reflected at the sample-holder slide. This total reflection generates an evanescent field, which must be manually adjusted to be of sufficient strength for nano-precision measurement, above the glass slide. A cantilever probe (NuNano Ltd.) is selected to be excited in the horizontal plane along the y-axis by a sine wave of amplitude approximately 2 nm at 200 kHz, which is around its first resonance in water.

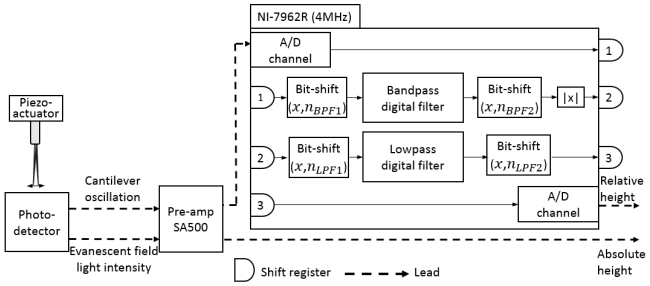

Fig. 3: The electronics design of sensing component.

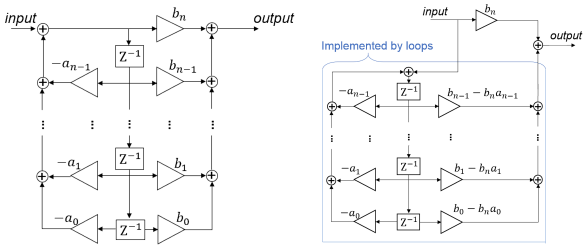

(a) Direct impl. (Sect. III) (b) Loop impl. (Sect. IV)

Fig. 4: Implementation structures of a digital filter $H(z) = [\sum_{k=0}^{n} b_{n-k} z^{-k}]/[1 + \sum_{k=1}^{n} a_{(n-k)} z^{-k}]$ in "direct form II transposed" structure.

In the evanescent field, the light field is scattered/reflected by the cantilever and the reflection of the excited cantilever is focused on a quadrant photo-detector. Due to the exponential decay of the evanescent wave with respect to distance, the reflected light intensity exponentially decreases when the cantilever moves away from the sample-holder slide.

Physically the ordered water layer covering the sample-substrate surface is a few nanometers (about 6 nm in this work) thick depending on the cantilever excitation and the environmental conditions. When the horizontally excited cantilever enters the confined water layer, the interacting shear-force changes the cantilever oscillation dynamics. The oscillation amplitude decreases as the distance between the cantilever and the sample-substrate becomes shorter. Thus, the photo-detector directly simultaneously measures two signals associated with the reflected light, i.e. two distance measurements along the vertical axis (z-axis):

- absolute height: the light intensity decreases with increasing the distance from the cantilever to the glass slide.
- relative height: a decrease of the distance between the cantilever and the sample-substrate relates to a lower amplitude of the cantilever oscillation.

The vertical axis positioning system consists of the optical sensing system, the cantilever, one horizontal and two vertical piezo actuators as shown in Figure 1. The vertical cantilever is extended from the lower edge of a Si_3N_4 chip mounted on a cantilever-probe holder. A dither piezo-actuator is attached to the holder to horizontally excite the cantilever along the y-axis. A coarse piezo-actuator places the oscillating cantilever into the sensing range. For feedback control, the vertical axis positioning component uses a fine piezo-actuator. The TDFM mechanical design follows the same design as in [17]. The piezo-actuation component is designed to hold the vertical cantilever-chip at the planar centre of the TDFM head mass. The TDFM head sits tightly above a TDFM base, which carries the horizontal positioning stage. The TDFM head and base is manufactured of aluminium alloy providing a high mass in comparison to the piezo-positioning system, so that the dynamic influence of the piezo-actuation components on the whole system is minimized.

III. Novel Sensing Component Design via FPGA

The sensing electronics component employs a pre-amplifier to boost the signals from the photo-detector (Figure 3). The light intensity is amplified 20 times and low-pass filtered with a 1 MHz cut-off frequency. The amplified signal is directly used as a measure of the absolute height. The cantilever oscillation signal is amplified by a gain of 500 and bandpass-filtered using a bandwidth region of 1 kHz - 1 MHz. The bandpass filtered signal is fed into a baseband transceiver to be processed by an NI-7962R FPGA board. On the FPGA board, (similar to the design concept in [19]), the digitized signal is bandpass filtered between 180 - 220 kHz to focus on the region around the excitation frequency, i.e. the influence of low frequency disturbances and high frequency electro-magnetic noise is partially eliminated. Then, a low-pass filter with a 60 kHz cut-off frequency is applied to the absolute value of the bandpass filtered signal. Finally, the averaged (low-pass filtered) absolute value of the oscillation signal, i.e. a measure of the signal amplitude, is sent to an analogue output channel as the measurement of the relative height.

A. Measurement signal processing on FPGA

An FPGA based solution is chosen in this work to achieve high sensing and control bandwidth. This is a powerful and still novel approach in the area of probe microscopy control [4], [20]. FPGA based design easily permits prototyping different digital circuit designs and promises reliability to run a control program at high sampling frequency. Fixed-point arithmetic is adopted as an efficient way to implement controllers on FPGAs [22] with the advantage of low computational resource cost and applicability for fast execution. However, there are practical issues to overcome: the fixed amount of binary gates and of DSP slices limits the numerical range and the calculation precision. Additionally, the implementation structure of complex functions (e.g. digital filters) determines the computational cost and the sampling time of the implemented controllers. In general, the program structure and fixed-point configuration also influence the quantization error and the time delay. Also, the overall running frequency has to meet the controllers' functionality requirements while considering the performance of the Analog-to-Digital (A/D) and Digital-to-Analog (D/A) channels.

Here, the oscillation amplitude averaging function is designed to run on the NI-7962R at a sampling frequency of 4 MHz considering the cantilever oscillation is at 200 kHz. This cycle time allows the execution of a second order transfer function, which is programmed in a "direct form II transposed" structure as a favoured structure in FPGA filter design [23]. Thus, the bandpass and lowpass filters are designed as two

second order Butterworth filters in parallel. Specifically, both the filters are implemented in the format shown in Figure 4a, in order to maximize the execution speed of the sensing program. In Figure 4a (and also Figure 4b), the delay z^{-1}, the gains, and additions are implemented by shift-register, multiplication, and addition operation in fixed-point arithmetic. For ease of implementation, every fixed-point arithmetic operation is configured as signed fxp-32-16 (i.e. 32 bits word length overall with 16 fractional bits) instead of optimizing each arithmetic operation and representation of all variables individually which could be considerably complex and time-consuming. At the input site of each digital filter, a bit-shift operation is introduced to avoid overflows and improve the numeric precision of each filter, specifically, $bit\text{-}shift(x, n_{BPF1})$ for the bandpass filter and $bit\text{-}shift(x, n_{LPF1})$ for the lowpass filter in Figure 3. Here, "$bit\text{-}shift(x, n)$" represents the zero-fill operation to bit-shift the input variable x by n binary bits with the sign preserved. Specifically, the digits of binary bit-shifts are presented by signed integers n_{E2C}, n_{Inter}, n_{C2O} in Figure 2 and signed integers n_{BPF1}, n_{BPF2}, n_{LPF1}, n_{LPF2} in Figure 3. The bit-shifts ($bit\text{-}shift(x, n_{BPF1})$ and $bit\text{-}shift(x, n_{LPF1})$) at the inputs of each filters are paired with the bit-shifts ($bit\text{-}shift(x, n_{BPF2})$ and $bit\text{-}shift(x, n_{LPF2})$) at the relevant filter outputs to set the combined gain of each pair to one, i.e. n_{BPF2}=$-n_{BPF1}$ and n_{LPF2}=$-n_{LPF1}$. As a result, the sensing solution is presented in Figure 3.

B. Enhancing the robustness of filters in fixed-point arithmetic

The fixed-point based signal processing programs work only within a limited fixed-point numerical range. Practically, the range is dynamically configurable by manipulating the bit-shift operations in each specific filter. It is vital to avoid any computational failure, which can be caused by overflows or the lack of computational accuracy. Thus, an offline optimization tool is suggested to assess the digital signal processing program designs prior to implementation.

The offline optimization tool is programmed in Simulink (Matlab, the MathWorks, Inc.). The arithmetic operations are simulated using the fixed-point toolbox and the practical time delays of the circuit to achieve an accurate replica of the practical implementation. Here, a suggested criterion to evaluate the appropriateness of a configuration (n_{BPF1}, n_{LPF1}) is to compare the output of the simulated digital filter $y_{(n_{BPF1}, n_{LPF1})}$ with an expected output signal y_{ref} over a simulation time of 0.1s. Demanding an input amplitude from 0 V to 2 V, the averaged absolute difference

$$|\bar{E}_{S(n_{BPF1}, n_{LPF1})}| = [\sum_{k=1}^{N} |y_{(n_{BPF1}, n_{LPF1})}(k) - y_{ref}(k)|]/N \quad (1)$$

at each sample time $k = 1, 2, .., N$ (at 4 MHz frequency) is used to evaluate the designs in Figure 5a. Among all the potential configurations (n_{BPF1}∈[-32,32], n_{LPF1}∈[-32,32]), it is clear that only a design within a limited optimal region consequently permits robust execution over the designed input range. For the FPGA program, the choice of (n_{BPF1},n_{LPF1}) = (-6,-6) and (n_{BPF2},n_{LPF2}) = (6,6) was made.

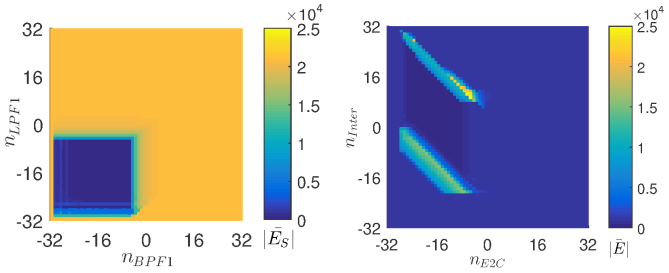

(a) Evaluation of ($|\bar{E}_s|$) for potential (n_{BPF1},n_{LPF1}) configuration in the sensing component design

(b) Evaluation of ($|\bar{E}_c|$) for potential (n_{E2C},n_{Inter}) configuration in the feedback control design

Fig. 5: Results demonstration of the suggested offline optimization for FPGA program design in fixed-point arithmetic.

IV. FPGA Based Real-time Control Solution

A. Vertical positioning systems and scan modes

The real-time control of the vertical axis positioning system is implemented (as in Figure 2) with an NI-7854R FPGA board. The digital control loop runs at a frequency of 500 kHz considering the maximum A/D channel sampling rate of 750 kHz. The absolute height and relative height measurements are both presented by signed $I16$-variables (16-bit integers) on the NI-7854R and the host-PC.

There are two height measurements possible for feedback control: either the light intensity measured from the photodetector (the absolute height above the glass slide) or the cantilever oscillation amplitude evaluation calculated from the NI-7962R board (the relative height with respect to the sample-substrate). The control reference is generated by a digital signal generator program onboard. The feedback control loop is made up by directly feeding the control error to a customizable control algorithm block, using fixed-point arithmetic based digital filters to implement transfer functions. The control signal (in signed $I16$ representation) drives the fine piezo-actuator. Hence, the vertical axis control has an actuation range of 440 nm with a resolution of about 0.067 nm per integer representation. In principle, the vertical axis control solution permits two scanning modes:

- constant relative height (CRH) scan: The absolute height is recorded as the topographic data while keeping a constant relative height to the sample-substrate.
- constant absolute height (CAH) scan: The cantilever is kept at a constant distance to the sample-holder slide. The top part (within the relative height sensing range below the scanning height) of the specimen is imaged.

B. Enhancing the robustness of digital control programs

The digital feedback control program has to be designed to be robust to disturbances and changes in environmental conditions. A rapid disturbance change may cause overflows in the fixed-point-arithmetic based digital filters. The strength of the evanescent field influences the measurement sensitivity and determines the range and the precision of the signals.

For control transfer functions implementation, this work exploits a bank of digital filters (i.e. two digital filter blocks

in Figure 2) in series. The overall 500 kHz clock frequency theoretically allows the execution of an up-to 6-th order digital filter, which employs loops to implement a digital filter in a cascaded biquad form. This maximizes the hardware usage (see Figure 4b) by sacrificing implementation speed. These two 6-th order digital filters are programmed to run in parallel. Each of the fixed-point-arithmetic operations (again shift-register, multiplication, and addition) is configured as signed fxp-32-16. Three bit-shift operations are introduced in the filter bank. Specifically, the bit-shift operations ($bit\text{-}shift(x, n_{E2C})$, $bit\text{-}shift(x, n_{Inter})$) are used to adjust the input range of the two digital filters to avoid overflows. In order to retain the designed control magnitudes, another $bit\text{-}shift(x, n_{C2O})$ is designed to compensate for the gain shift from the other two bit-shifts. At the output of the filter bank, a tunable gain $Gain$ is introduced, to be adjusted to take into account the change of the measurement sensitivity of the evanescent field sensing system. With respect to particular digital filter designs, the zeros and poles of a transfer function have to be carefully distributed into two digital filter blocks to avoid overflows and achieve high numerical accuracy.

Thus, complex controllers, associated with robust control, are implementable at a fast clock frequency with some design flexibility. Typical FPGA designs for control usually require the optimization of each single fixed-point arithmetic operation and their parameters in an implemented digital program and relevant digital filters. In the majority of the cases, the FPGA board must be stopped and reloaded with the reconfigured fixed-point implementation when the controller needs to be changed (e.g. [21]). In contrast, the proposed design configures all operations to be consistent fixed-point representations (i.e. signed fxp-32-16) and only the bit-shift operations are adjusted to achieve a good control performance with respect to different controllers. Therefore, the value of the control coefficients and optimized bit-shifts can be changed online without the necessity of reconfiguring any fixed-point arithmetic/representation, i.e. there is no need to reload the FPGA board. This results in a significant benefit in terms of flexibility for online reconfiguration of the digital filters with the same digital implementation. Specifically, the controllers for the absolute height and relative height can be switched online at low hardware cost. Also, the control programs are robust enough for practical scans via the following proposed optimization procedure.

The configuration of (n_{E2C}∈[-32,32], n_{Inter}∈[-32,32]) determines the numerical working range of the digital feedback control loop. The functional computational range is bounded, once the filter bank coefficients and $Gain$ are decided. The proposed offline optimization tool is applied to guarantee the feedback control performance in practice. The optimization criterion involves selecting a pair of (n_{E2C}, n_{Inter}), which minimizes the control error $e_{(n_{E2C},n_{Inter})}$, tracking a reference over a period of 1s. In particular, the reference signals are set as square waves with a period of 10 Hz and fixed amplitude. All potential (n_{E2C}, n_{Inter}) selections are assessed by the averaged absolute control error

$$|\bar{E_c}|_{(n_{E2C},n_{Inter})} = (\sum_{k=1}^{N} |e_{(n_{E2C},n_{Inter})}(k)|)/N \qquad (2)$$

at all sampling instances ($k = 1, 2, ..., N$ at a sampling rate of 500 kHz) during the simulation. This allows the minimization of the effect due to quantization of the controller. An optimization result is presented in Figure 5b as an example, where the controller follows, in this specific case, a lag control paradigm (as in Section VI-A). Giving a reference amplitude of 1000, it is clear that the selected pairs of (n_{E2C}, n_{Inter}) significantly influence the feedback performance.

V. Absolute Height Positioning Control

A. Plant system identification

The sensing curve of the absolute height measurement versus the cantilever position (away from the glass slide) is measured 20 times as shown in Figure 6. It is known that the evanescent field wave strength decays exponentially with distance [15] (as confirmed here). Note that the absolute height measurement sensitivity depends on the optical path, which is specifically adjusted at the beginning of each experiment. Thus, the sensing curve has to be calibrated every time after the optical path is prepared for each experiment.

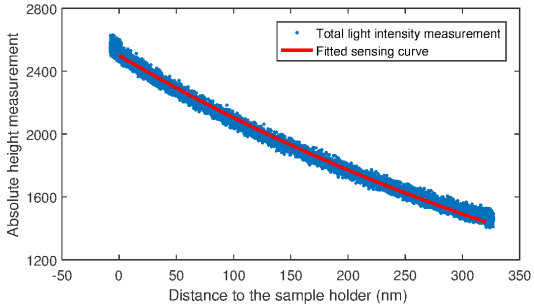

Fig. 6: Absolute height sensing curve.

The plant frequency response is identified by employing the swept-sine method with an excitation amplitude of 0.5 V (equating 1.2 nm) as shown in Figure 7. The measured plant response includes the computation and other hardware delays (overall ∼8 μs). The plant has a constant magnitude and little phase delay in the low frequency region. There are resonances appearing at 5 kHz, 6 kHz, 10.5 kHz, 30.5 kHz, and at various higher frequencies. It has been decided that the plant model is to fit only the first four resonances: any dynamics above 40 kHz are regarded as uncertainty.

B. H_∞ control design

Robust H_∞ control is selected since the plant has a varying gain at low frequency and a high-level of uncertainty in the high frequency range. Here notch filters are not feasible because of the high computational cost for multiple high-performance notch-filter implementations. An H_∞ mixed-sensitivity synthesis is used to design a robust controller using the Robust Control Toolbox in Matlab.

In the design, the sensitivity S_{AH} is shaped to achieve good disturbance attenuation (Figure 8). The complementary

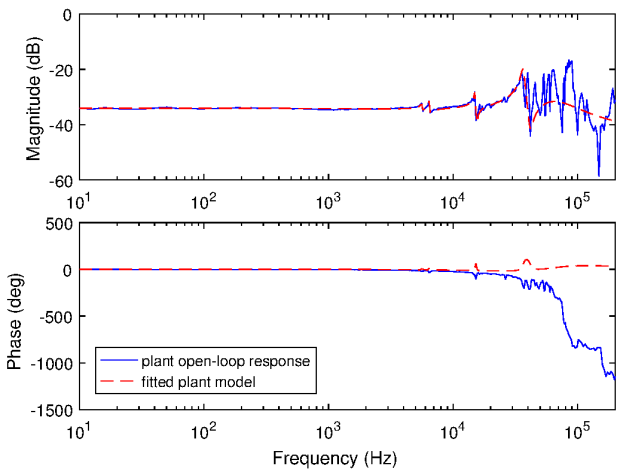

Fig. 7: Absolute height plant frequency response using open-loop system identification.

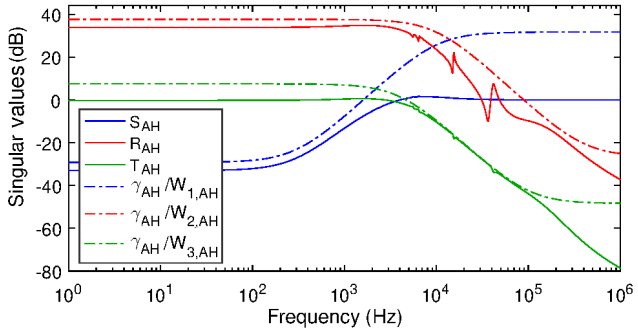

Fig. 8: Mixed-sensitivity design for the absolute height control where γ_{AH} is the closed-loop H_∞ norm. Weights $W_{1,AH}$, $W_{2,AH}$, and $W_{3,AH}$ are designed for the sensitivity S_{AH}, the control effort R_{AH}, and the co-sensitivity T_{AH} respectively.

sensitivity T_{AH} is designed to remain between 0 dB and -3 dB until about 5 kHz (below the first resonance). The transfer function of the product of the sensitivity and the controller, the control effort $R_{AH} = S_{AH}C_{AH}$, is designed to suppress the uncertainty over 40 kHz. The weighting functions $W_{1,AH}$, $W_{2,AH}$, and $W_{3,AH}$ corresponding to S_{AH}, R_{AH}, and T_{AH} are designed as shown in Figure 8. The obtained controller is model-reduced to a 6th-order transfer function using a DC gain matching method (*modred* function in Matlab). The open-loop system has a gain margin of 24 dB at 29.9 kHz and the phase margin is 67.2° at 3.53 kHz (Figure 9).

The continuous time controller is discretized using Tustin's method at a sampling frequency of 500 kHz. In practice, the discrete controller is split into two discrete transfer functions:

$$C_{AH,1}(z) = \frac{0.999z^2 - 1.96z + 0.995}{z^2 - 1.96z + 0.995}$$
$$C_{AH,2}(z) = \frac{1.16z^3 - 3.48z^2 + 3.86z - 1.53}{z^3 - 2.84z^2 + 2.68z - 0.842} \quad (3)$$

The bit-shift operations have been optimized offline as (n_{E2C}, n_{Inter}, n_{C2O}) = (-13,5,8).

C. Robust control performance

In the experiments, the cantilever is placed at 5 nm above the sample-holder glass slide. To examine the tracking performance, a square wave reference is applied to drive the

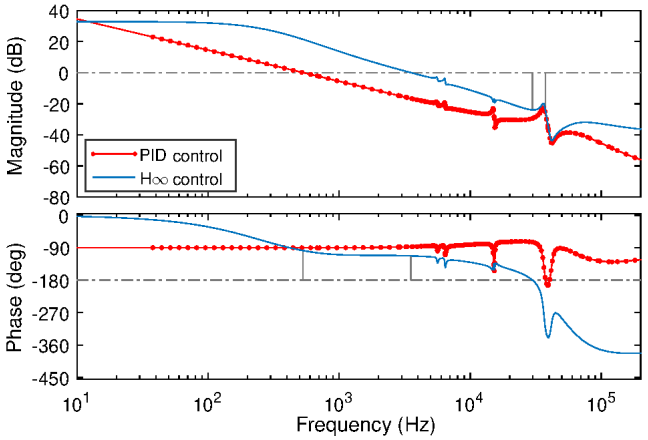

Fig. 9: Absolute height open-loop response using the model reduced H_∞ controller or the optimized PID controller.

cantilever with a step size of 100 (i.e. about 50 nm distance) at 1 kHz, controlling the absolute height. The absolute height controller has a settling time of less than 0.3 ms satisfying the H_∞ control design (Figure 10a and 10b). The closed-loop system is also tested to track a reference with about 1 nm step-size at 1 kHz frequency, where noisy measurements are predominant (see Figure 10b). In the CAH scan mode, the controller only needs to respond to small changes due to the roughness of the sample-holder slide that is often a flat surface.

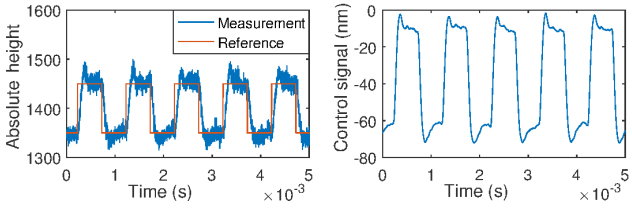

(a) Tracking a square wave with 100 absolute height (≈ 50 nm) step size.

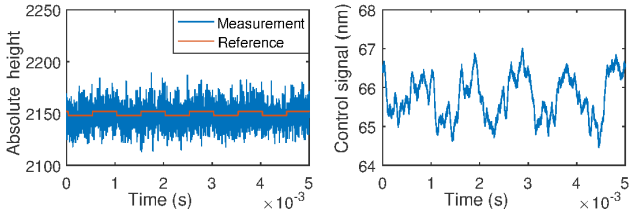

(b) Tracking a square wave with 2 absolute height (≈ 1 nm) step size.

Fig. 10: Absolute height tracking performance employing the H_∞ control for 1 kHz square wave demands.

In comparison to a classic PID control, the proposed H_∞ control method brings the following advantages. The H_∞ control has a faster response and reacts better and more robustly at high-frequency as shown in Figure 11. This means the H_∞ controller provides a better scanning performance in terms of retaining a constant absolute height in comparison to a PID controller, usually used for the TDFM (and other probe microscopes [15], [17], [20]). Here, an optimized PID controller can be obtained via structured H_∞ synthesis [24], by applying weighting functions similar to the H_∞ design in Figure 8. The PID controlled open-loop system has a gain margin of 28.8 dB at 3.76 kHz and a phase margin of 89.9° at 0.4 kHz (see Figure 9). Moreover, an analogue low-pass

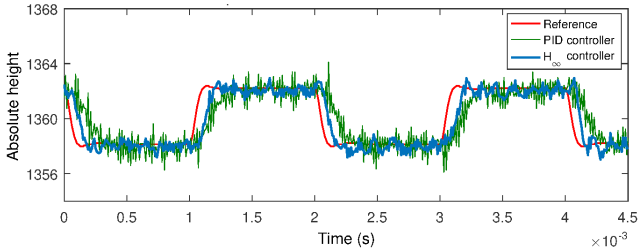

Fig. 11: Absolute height tracking performance using the PID and the H_∞ controller to track a low-pass filtered square wave at 500 Hz with a step size of 4 absolute height ($\approx$ 2 nm)

filter with 200 kHz cutoff frequency is applied to the absolute height measurement in Figure 11. In the high frequency region above 100 kHz, this low-pass filter introduces an additional lag, which is needed for the PID control scheme to reduce the strong noise affect and to avoid the uncertainties at high frequencies above 100 kHz. Overall, the applied PID-controller is the most suited as a gain increase would cause instability due to the unmodelled uncertainty (see also the small, remaining oscillations in Figure 11). However, the H_∞ controller works without needing an extra lag-filter. Another benefit of using the H_∞ controller is the ease of use: With sufficient knowledge on the absolute height positioning system, only one gain in the H_∞ controller needs to be adjusted for the control signal when the optical path is readjusted (e.g. due to a change of the glass-slide). In contrast, the previous TDFM [17] design which only employs an ad-hoc tuned PID control needs significant operational expertise in practice.

VI. Relative Height Positioning Control

A. Plant system identification

Precise relative height sensing curves are not measurable in open-loop due to the significant influence of Brownian motion, electrical noise, and disturbances. Hence, the relative height sensing curve, which is represented by the cantilever oscillation amplitude measurement as a function of the cantilever distance to the sample-substrate (see Figure 3 and 12), is measured 20 times employing the absolute height control.

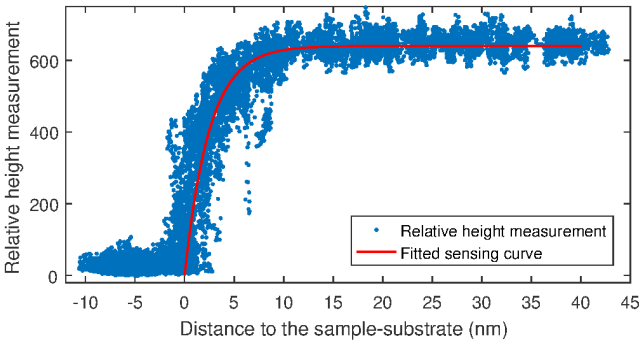

Fig. 12: Relative height sensing curve.

The partial discontinuity and high uncertainty of this measurement curve (Figure 12) is for two reasons: a) Brownian motion and b) the lattice-like structure of the confined water layer just above the specimen. (This water layer creates molecule lattices through which the cantilever traverses. Passing through each lattice causes a discontinuity in the amplitude measurement, as observed here for a $\sim$6 nm range.) Thus, the sensing nonlinearity and the uncertainty in addition to the plant dynamics have to be carefully considered in the control design.

Precise relative height positioning system dynamics have been identified in a closed-loop manner. For this, a lag controller was designed using initial plant measurements obtained in open-loop. The relative height open-loop response with the lag controller has a gain margin of 16.5 dB at 3.5 kHz and a 77.1° phase margin at 2.5 kHz. The open-loop response is given in Figure 15 with control performance examples in Figure 16. From Figure 15, it is evident that the lag control provides (with its structural limits) a similar performance as the H_∞ controller (to be designed in Section VI-B). And an increase of the open-loop gain would damage robust performance. This allows now to measure the plant response in closed-loop at different relative heights (from 150 to 550 relative height with a step size of 50). The measured responses exhibit differences in magnitudes in the low frequency range at each offset (see examples in Figure 13). Note that the measurements are affected by noise (as discussed earlier) which was also not easily suppressed by averaging the response. Despite this, it is clear that at each height the low frequency gain keeps constant until about 3 kHz. The magnitudes of the plant response at each operation height gradually converges to a similar shape in the high frequency range from 11 kHz to 200 kHz. At different relative heights, the low frequency gain of the plant begins from -8 dB at 150 relative height, increases to 10 dB at 300 until 400 relative height, then drops to about -5 dB at 550 relative height. The plant response at high frequency has a magnitude no more than 15 dB at all operational positions.

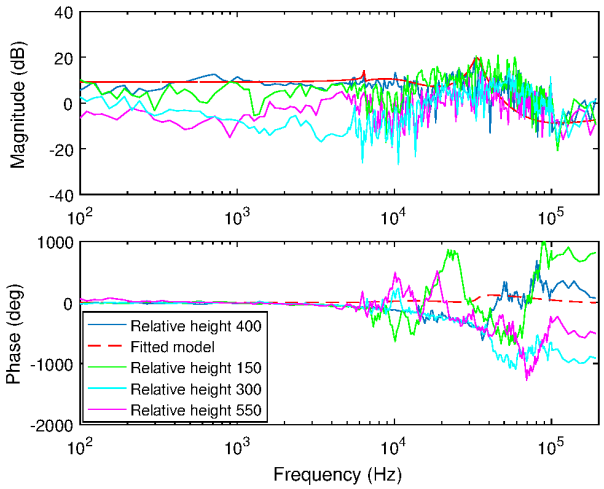

Fig. 13: Relative height plant frequency response measured at 150, 300, 400, 550 relative height using the closed loop identification method, and a fitted model for control design.

B. H_∞ control design

In contrast to constant absolute height feedback, the relative height control has to keep a constant distance to the sample-substrate without contacting the specimens. Hence, it must be

noted that the sample topography may rapidly change over the whole scan frame. The strong plant nonlinearity significantly influences both the magnitude and the phase of the closed-loop control performance. Control solutions designed using simple frequency domain shaping methods cannot rapidly tackle dynamic scanning tasks in practice. Thus, a mixed sensitivity H_∞ control design is suggested for two reasons: a) an appropriate low-frequency sensitivity and sufficient bandwidth at various relative heights; and b) the suppression of uncertainty in the high frequency region. The plant is modelled by the response at 400 relative height (i.e. about 3 nm over the sample-substrate in experimental scans).

Robustness to high frequency uncertainty is achieved considering the measured plant frequency response and by shaping sensitivity, co-sensitivity, and the control effort to obtain a fast roll-off. Also, the conservative design guarantees sufficient robustness to the varying plant response below 3 kHz. For the mixed-sensitivity H_∞ design, three weights $W_{1,RH}$, $W_{2,RH}$, and $W_{3,RH}$ are chosen for the sensitivity S_{RH}, the control effort R_{RH}, and the co-sensitivity T_{RH} respectively (see Figure 14). After using a DC gain matching model reduction method for controller order reduction, the open-loop response (Figure 15) has a phase margin of 58.7° at 1.99 kHz.

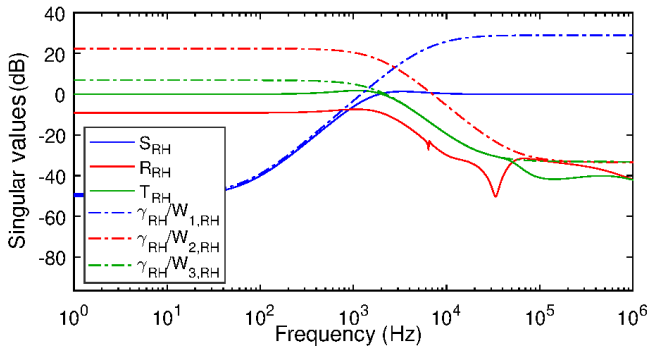

Fig. 14: Mixed-sensitivity design for the relative height control where γ_{RH} is the closed-loop H_∞ norm. Weights $W_{1,RH}$, $W_{2,RH}$, and $W_{3,RH}$ are designed for the sensitivity S_{RH}, the control effort R_{RH}, and the co-sensitivity T_{RH} respectively.

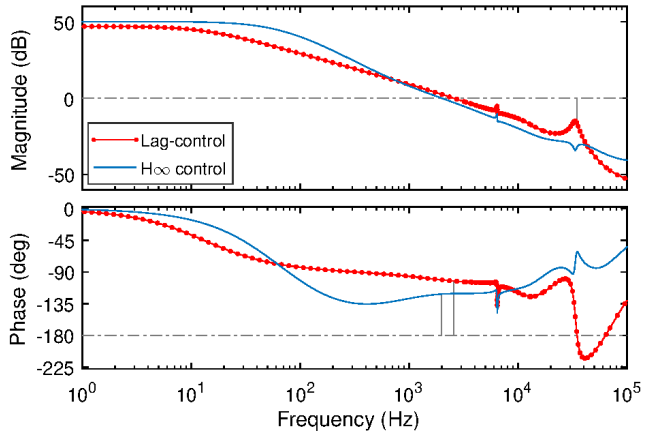

Fig. 15: Relative height controller open-loop response with the model reduced H_∞ controller or the designed lag-controller.

Here the 7th order H_∞ controller is discretized (using the Tustin's method) and split into two transfer functions for implementation on the NI-7854R:

$$C_{RH,1}(z) = \frac{0.0195z^4 - 0.0138z^3 - 0.0220z^2 + 0.0153z + 0.00162}{z^4 - 1.68z^3 + 0.201z^2 + 0.693z - 0.216} \quad (4)$$

$$C_{RH,2}(z) = \frac{0.805z^3 - 2.25z^2 + 2.22z - 0.774}{z^3 - 2.42z^2 + 2.03z - 0.606}$$

The bit-shift operations are offline optimized as (n_{E2C}, n_{Inter}, n_{C2O}) = (-19, 8, 11).

C. Robust control performance

The H_∞ controller is assessed by tracking a square wave reference with an amplitude of 50 at a frequency of 300 Hz at relative heights of 200, 300, 500 as shown in Figure 16. The controller achieves a closed loop bandwidth of about 2 kHz, robust to different relative heights. In contrast, the lag-controller fails to obtain the designed 1 kHz bandwidth at a relative height of 200 and 500. The robust control design decoupled the noise signal well and achieved a vertical resolution of 1 nm. The robustness of the H_∞ control performance is also nicely visible from the smooth control signal for this noise predominant control challenge as Figure 17 shows.

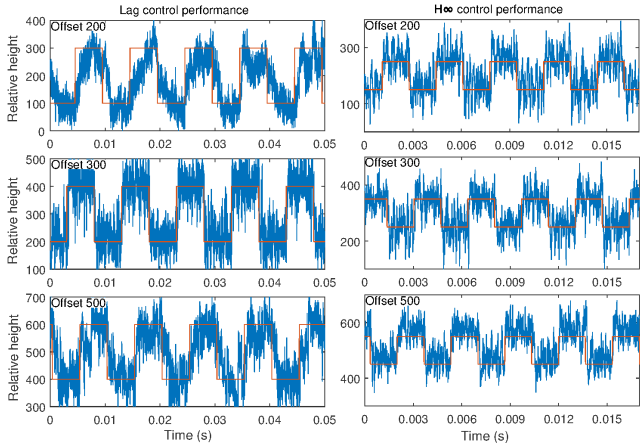

Fig. 16: Relative height tracking performance employing the lag controller (left column) for a square wave reference with an amplitude of 100 relative height at 100 Hz frequency and H_∞ controller (right column) for a square wave reference with an amplitude of 50 relative height at 300 Hz frequency at relative height of 200, 300, and 500.

To address the contribution of the H_∞ control to the performance, the steady state performance characteristics of the lag controller and the H_∞ controller are compared with the open-loop measurement of the relative height sensor. In each case, the cantilever tip is placed at the relative heights of 100, 200, 300, 400, and 500 over the sample-substrate. 5000 samples are taken at each height for each of the three different cases. In Figure 18, the normalized histogram shows that the open-loop regime cannot sufficiently guarantee a constant value. In contrast, the lag control and the H_∞ control significantly improve the positioning accuracy. In detail, the lag control result has only at two relative height values of 100 and 500 the smallest standard deviation, while at all other heights, the H_∞ control has superior performance. The consistent performance of the H_∞ control, i.e. it shows the robust stability and performance to the varying plant dynamics.

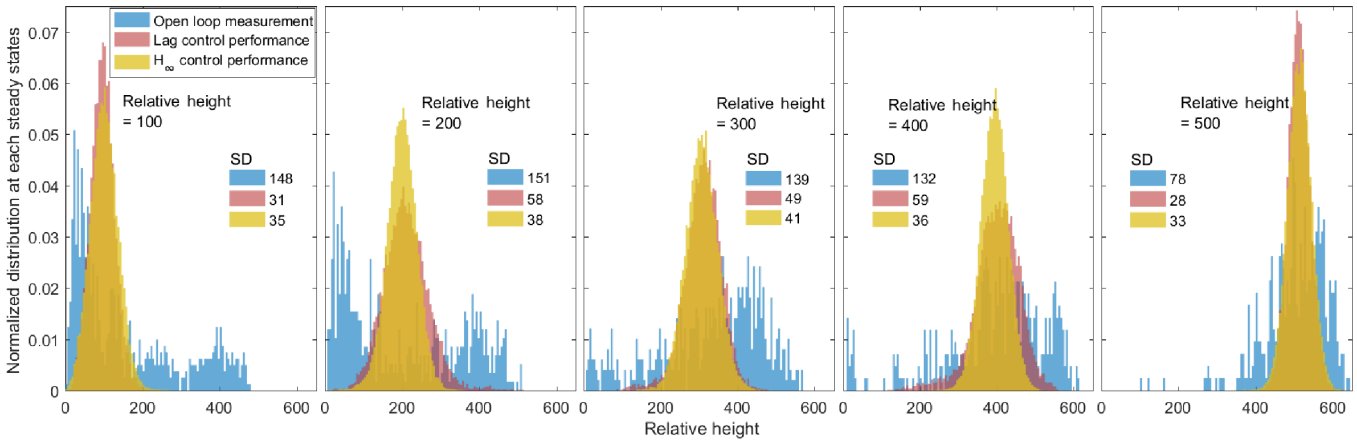

Fig. 18: The normalized histogram of relative height measurement at each relative height references (at 100, 200, 300, 400, and 500) in open-loop, the lag-controlled feedback loop, and the H_∞-controlled feedback loop. 'SD' indicates the standard deviation of the relative height measurements with respect to the expectation in each case.

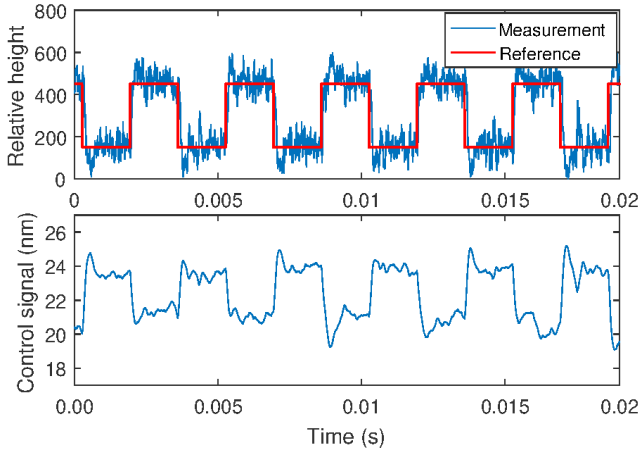

Fig. 17: Relative height H_∞ tracking control for a square wave reference at 300 Hz from 150 to 450 relative height.

VII. CAH & CRH Feedback Mode Scans

To assess the imaging performance, samples with standard shapes are selected: specifically polymer microspheres (R50, Fluoro-Max, Thermo Fisher Scientific Inc.) with a nominal diameter of 50 nm. The specimen solution is prepared in purified water buffer with a 10 mM/L concentration of nano-sphere solution and a 10 mM/L concentration of $NiCl_2$, which creates salt bridges, bonding the nano-spheres to the glass slide. All the scans in this paper apply 20 μl specimen solution on the glass slide. All presented experiments scan 400 nm $\times$ 400 nm areas at a resolution of 2 nm/pixel and at a scanning speed of 1.6 μm/s. The topographic height measurement in nanometers is calibrated by the practical sensing curves in each experiment.

In CAH scan mode, the cantilever is kept at about 50 nm above the sample-holder slide (Figure 19). Thus, only the very top part of each nano-sphere is imaged within the relative height sensing range ($\sim$6 nm) in the scans. Both the trace and retrace images are generated by either the forth and back motion scans along the x-axis. The similarity between the trace and the retrace images indicates the success of the absolute height control and the scan regime. In the horizontal plane, the imaged particles have the shapes of circles with diameters less than 33 nm, which fits the dimension of the spherical cross sections at the scanning height. The vertical height of the imaged particles also approximates 50 nm as expected.

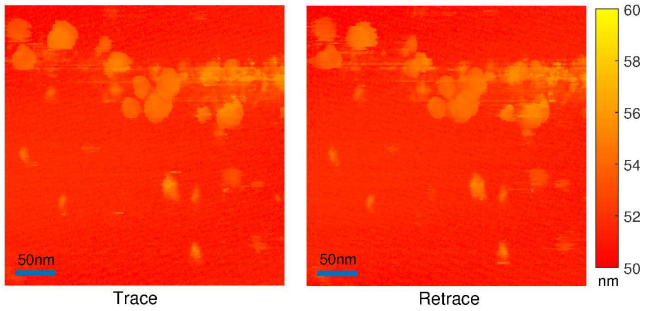

Fig. 19: Constant absolute height scan results.

Practically, the cantilever in CRH scans is kept at a 400 relative height (about 3 nm) over the sample-substrate (Figure 20). The topographical image is obtained from the absolute height sensing signal. The similarity between the trace and re-trace images shows that the relative height controller performs robustly providing good CRH-scan results. The specimen spheres have a diameter of about 50 nm along the vertical axis and in the horizontal plane. Thus, it is evident that the developed CRH scanning approach successfully provides precise topography measurements.

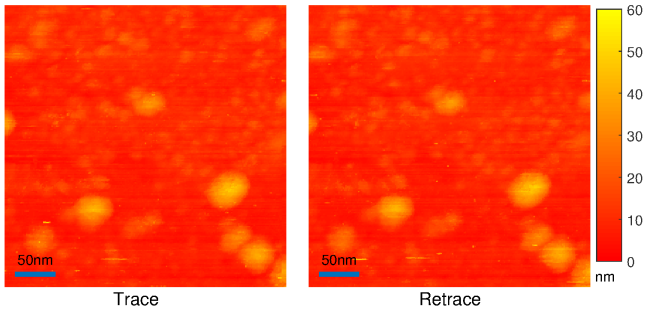

Fig. 20: Constant relative height scan results.

The CRH and CAH scan modes are applied to the same area for comparison. The trace images in the two scanning modes are shown in Figure 21. The scanned area is initially imaged in the CRH mode providing the detailed topography of the scanned region. In contrast, the CAH scan images only the top of the largest particle in the same frame. The CAH-scan requires a priori-knowledge about the height of the specimen so as to approach only the very top of the specimen and to carefully scan the cusps. A meticulous downward motion and repeated scans can then capture more detail with the CAH-scan. In contrast, the CRH scan can provide the topographic details of the sample-substrate from one single scan. In practice, both scan approaches achieve a resolution of 1 nm along the z-axis with the designed controllers.

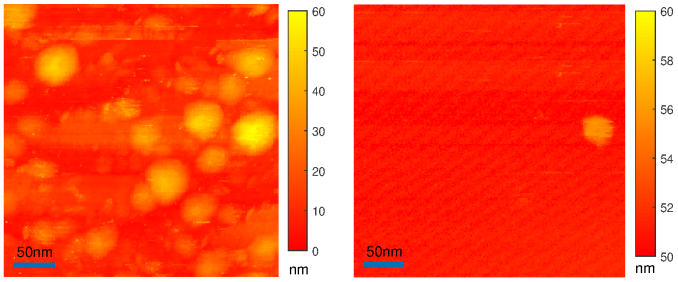

Fig. 21: Comparison of CRH (left) and CAH (right) modes.

VIII. Discussions

The TDFM control hardware has been improved by deploying a novel easily optimized Control and Instrument structure using FPGAs. The digital control program has the advantage of permitting online reconfigurability while maximizing the hardware efficiency. An offline optimization method has been developed for the digital sensing and control programs in order to enhance the programming robustness for practical scanning.

Robust H_∞ control design has, for the first time, been introduced into the TDFM's vertical positioning mechanism: the absolute height control and the relative height control. The proposed H_∞ control methods have shown superior performance for both positioning systems when compared to PID control and lag-control respectively.

The improved vertical positioning performance practically benefits the scanning performance of the TDFM. In particular for the CAH mode, the imaging noise peak-to-peak level is reduced from 0.8 nm to 0.5 nm due to the improved positioning performance of the H_∞ controller in relation to the PID control. By introducing the H_∞ controller, the CRH mode has a sufficient imaging contrast to observe the $\sim$50 nm height of the sample spheres. In contrast, the CRH mode employing the lag-controller loses one third imaging contrast, because the lag-control is unable to tackle the plant nonlinearity during dynamic scans. Importantly, practical scans show that the CAH mode with the new sensing system increases the imaging range up to 6 nm from about 2 nm in the experimental conditions. Also the CRH mode is capable of scanning specimens of at least 50 nm height in one scan.

IX. Conclusions and Future Work

The paper introduces an integrated TDFM system for vertical cantilever positioning control, which facilitates raster scanning to image nano-particles at nano resolution. The combined mechanical/electronic design of the integrated embedded system was introduced. The optical sensing curves and vertical plant dynamics have been studied in the frequency domain. The nonlinearity in the TDFM sensing mechanism has been identified and compensated by an H_∞ controller.

Two scanning modes of the TDFM, including a constant absolute height (CAH) mode and a constant relative height (CRH) mode, are developed and compared. The CAH mode is a fast topography scanning approach which requires some prior detailed understanding of the sample height/topography. In contrast, the CRH mode is capable of scanning the whole sample-substrate – providing much more details of the scanned area. In future, the TDFM will be integrated with a high-speed stage to allow fast x-y scanning speed.

References

[1] G. Binnig, C. F. Quate, and C. Gerber, "Atomic force microscope," *Phys. Rev. Lett.*, p. 930, 1986.

[2] N. Chuang, I. R. Petersen, and H. R. Pota, "Robust H$_\infty$ control in fast atomic force microscopy," *Asian J. Control*, pp. 872–887, 2013.

[3] J. Ren, Q. Zou, B. Li, and Z. Lin, "High-speed atomic force microscope imaging: Adaptive multiloop mode," *Phys. Rev. E*, p. 012405, 2014.

[4] S. Kuiper, P. Van den Hof, and G. Schitter, "Integrated design of the feedback controller and topography estimator for atomic force microscopy," *Control Eng. Pract.*, pp. 1110–1120, 2013.

[5] E. Thormann, T. Pettersson, J. Kettle, and P. M. Claesson, "Probing material properties of polymeric surface layers with tapping mode AFM: Which cantilever spring constant, tapping amplitude and amplitude set point gives good image contrast and minimal surface damage?" *Ultramicroscopy*, pp. 313–319, 2010.

[6] V. Vahdat and R. W. Carpick, "Practical method to limit tip–sample contact stress and prevent wear in amplitude modulation atomic force microscopy," *ACS nano*, pp. 9836–9850, 2013.

[7] E. Betzig, P. Finn, and J. Weiner, "Combined shear force and near-field scanning optical microscopy," *Appl. Phys. Lett.*, pp. 2484–2486, 1992.

[8] M. Antognozzi, A. Humphris, and M. Miles, "Observation of molecular layering in a confined water film and study of the layers viscoelastic properties," *Appl. Phys. Lett.*, pp. 300–302, 2001.

[9] J.-K. Leong and C. Williams, "Shear force microscopy with capacitance detection for near-field scanning optical microscopy," *Appl. Phys. Lett.*, pp. 1432–1434, 1995.

[10] K.-D. Park *et al.*, "Operation of a wet near-field scanning optical microscope in stable zones by minimizing the resonance change of tuning forks," *Nanotechnology*, p. 075704, 2014.

[11] A. La Rosa, X. Cui, J. McCollum, N. Li, and R. Nordstrom, "The ultrasonic/shear-force microscope: Integrating ultrasonic sensing into a near-field scanning optical microscope," *Rev. Sci. Instrum.*, p. 093707, 2005.

[12] K. Karrai and I. Tiemann, "Interfacial shear force microscopy," *Phys. Rev. B*, p. 13174, 2000.

[13] P. Sandoz, J.-M. Friedt, and E. Carry, "Vibration amplitude of a tip-loaded quartz tuning fork during shear force microscopy scanning," *Rev. Sci. Instrum.*, p. 086102, 2008.

[14] L. M. de Lépinay, B. Pigeau, B. Besga, P. Vincent, P. Poncharal, and O. Arcizet, "A universal and ultrasensitive vectorial nanomechanical sensor for imaging 2D force fields," *Nat. Nanotechnol.*, p. 156, 2017.

[15] M. Antognozzi, A. Ulcinas, L. Picco, S. Simpson, P. Heard, M. Szczelkun, B. Brenner, and M. Miles, "A new detection system for extremely small vertically mounted cantilevers," *Nanotechnology*, p. 384002, 2008.

[16] J. M. Fletcher, R. L. Harniman, F. R. Barnes, A. L. Boyle, A. Collins, J. Mantell, T. H. Sharp, M. Antognozzi, P. J. Booth, N. Linden *et al.*, "Self-assembling cages from coiled-coil peptide modules," *Science*, pp. 595–599, 2013.

[17] R. Harniman, J. Vicary, J. Hörber, L. Picco, M. Miles, and M. Antognozzi, "Methods for imaging dna in liquid with lateral molecular-force microscopy," *Nanotechnology*, p. 085703, 2012.
[18] M. Antognozzi, A. Protti, M. Miles, and G. Valdrè, "Investigation of nano-confined liquids on muscovite by transverse dynamic force microscopy (TDFM)," *GeoActa*, pp. 101–106, 2003.
[19] T. Hatano, K. Zhang, S. Khan, T. Nguyen, G. Herrmann, C. Edwards, S. Burgess, and M. Miles, "A specimen-tracking controller for the transverse dynamic force microscope in non-contact mode," in *Proc. Am. Control Conf., 2016*, pp. 7384–7389. IEEE, 2016.
[20] I. Soltani Bozchalooi, "Design and control of high-speed and large-range atomic force microscope," Ph.D. dissertation, Mass. Inst. Techn., 2015.
[21] Z. Fang, J. E. Carletta, and R. J. Veillette, "A methodology for fpga-based control implementation," *IEEE Trans. Control Syst. Technol.*, p. 977, 2005.
[22] E. Monmasson and M. N. Cirstea, "FPGA design methodology for industrial control systems a review," *IEEE Trans. Ind. Electron.*, pp. 1824–1842, 2007.
[23] L. Harnefors, "Implementation of resonant controllers and filters in fixed-point arithmetic," *IEEE Trans. Ind. Electron.*, p. 1273, 2009.
[24] P. Gahinet and P. Apkarian, "Structured H_∞ synthesis in matlab," *IFAC Proceedings Volumes*, vol. 44, no. 1, pp. 1435–1440, 2011.